



Title	Highly Ordered Nanoscale Film Morphologies of Block Copolymers Governed by Nonlinear Topologies
Author(s)	Ree, Brian J.; Satoh, Yusuke; Isono, Takuya; Satoh, Toshifumi
Citation	ACS macro letters, 10(7), 811-818 https://doi.org/10.1021/acsmacrolett.1c00204
Issue Date	2021-07-20
Doc URL	http://hdl.handle.net/2115/85842
Rights	This document is the Accepted Manuscript version of a Published Work that appeared in final form in ACS Macro Letters, copyright c American Chemical Society after peer review and technical editing by the publisher. To access the final edited and published work see https://pubs.acs.org/articlesonrequest/AOR-UJNHY76MCFY32PBB3KGC .
Type	article (author version)
File Information	BJR-manuscript-revised-2.pdf



[Instructions for use](#)

Highly Ordered Nanoscale Film Morphologies of Block Copolymers Governed by Nonlinear Topologies

Brian J. Ree¹, Yusuke Satoh², Takuya Isono¹ and Toshifumi Satoh^{1,*}

¹ Graduate School of Chemical Sciences and Engineering, Hokkaido University, Sapporo 060-8628, Japan

² Faculty of Engineering, Hokkaido University, Sapporo 060-8628, Japan

*Correspondence to: satoh@eng.hokudai.ac.jp (T.S.)

ABSTRACT: Among many properties of cyclic block copolymers, the notable domain spacing (*d*-spacing) reduction offers nonlinear topology as an effective tool for developing block copolymers for nanolithography. However, the current consensus regarding the topology-morphology correlation is ambiguous and in need of more studies. Here we present the morphological investigation on nanoscale films of cyclic and tadpole-shaped poly(*n*-decyl glycidyl ether-*block*-2-(2-(2-methoxyethoxy)ethoxy)ethyl glycidyl ether)s and their linear counterpart *via* synchrotron grazing-incidence X-ray scattering. All copolymers form phase-separated nanostructures, in which only the nonlinear copolymers form highly ordered and unidirectional nanostructures. Additionally, *d*-spacings of cyclic and tadpole-shaped block copolymers are 49.3%–53.7% and 25.0%–32.5% shorter than that of their linear counterpart, respectively, exhibiting greater or comparable *d*-spacing reductions against the experimentally and theoretically achieved values from the literature. Overall, this study demonstrates that cyclic and tadpole topologies can be utilized in developing materials with miniaturized dimensions, high structural ordering, and unidirectional orientation for various nanotechnology applications.

Pioneering work on cyclic polymers dates back to 1946 when cyclic poly(dimethylsiloxane) was reported as the first synthetic cyclic polymer.¹⁻³ In 1949, Zimm and Stockmayer theoretically estimated an ideal, flexible cyclic polymer to exhibit a shorter radius of gyration than its linear analogue of the same molecular weight.⁴ Then, 1962 onwards, studies on cyclic deoxyribonucleic acids,⁵⁻⁸ cyclic proteins,^{9,10} and cyclic polysaccharides¹¹ inspired new synthetic methods for producing various cyclic homopolymers with high yield and purity.¹²⁻²⁷ Many reports have discussed the absence of chain ends as the primary reason for the unique physical properties of cyclic polymers, such as higher glass transition temperature, higher melting temperature, and lower viscosity than the linear counterparts.^{18-22,26-39}

In addition to homopolymers, many synthetic strategies producing various cyclic block copolymers have been reported.^{17-19,29,30,40-45} However, there is only a handful of reports exploring the topological influence on phase-separated morphological features in bulk state.^{40,46-49} Based on those reports, the consensus is that cyclic block copolymers form the same type of nanostructure as their linear counterpart, but with a 5%–16% shorter domain spacing (*d*-spacing).⁴⁶⁻⁴⁸ Interestingly, these experimentally observed *d*-spacing reductions are lesser than the theoretical predictions of 30%–37%.⁴⁹⁻⁵¹ Moreover, some studies reported controversial results where different nanostructures were observed between cyclic and linear iterations of poly(styrene-*block*-isoprene)⁵² and poly(styrene-*block*-butadiene).⁴⁶ Compared to bulk state, there are fewer investigations on nanoscale film morphologies. One report discusses hexagonally packed cylinders formed by both cyclic and linear poly(styrene-*block*-ethylene oxide)s (PS-*b*-PEO), where cyclic PS-*b*-PEO exhibits a 33% shorter *d*-spacing than that of linear PS-*b*-PEO.⁵³ This *d*-spacing reduction agrees with the theoretical prediction;⁴⁹⁻⁵¹ however, we have previously achieved 51.3%–72.8% *d*-spacing reduction and characterized different morphological types.⁵⁴ The report, however, is based on bicyclic topology, not cyclic. Nonetheless, the fact that there are only two reports investigating nanoscale film morphologies

of cyclic block copolymers indicates the need for additional studies. Overall, synthesis of cyclic block copolymers has progressed significantly, and the correlations among cyclic topology, chemical composition, physical properties, and morphology need further investigation. Particularly, morphology remains as the least explored aspect of cyclic block copolymers.

In this study, we report the first quantitative investigation of nanoscale film morphologies of poly(*n*-decyl glycidyl ether-*block*-2-(2-(2-methoxyethoxy)ethoxy)ethyl glycidyl ether)s (PDGE-*b*-PTEGGE) with cyclic and tadpole topologies—*cy*-BCP, *tp-A*-BCP, and *tp-B*-BCP (Figure 1; Table S1 in Supporting Information)—using synchrotron grazing-incidence X-ray scattering (GIXS). This quantitative study provides detailed structural parameters and discusses the correlation between molecular topology and morphological features. All the block copolymers are synthesized with a narrow dispersity (D) of 1.04, and they phase-separate into nanostructures driven by the immiscibility between PDGE and PTEGGE blocks. Despite nearly equivalent volume fractions (degree of polymerization for each block is approximately 50), all the copolymers form either distorted hexagonal cylindrical or lamellar structures, a unique behavior deviating from the aforementioned consensus and conventional volume fraction rule. For each copolymer, the d -spacing varies significantly with topology. *cy*-BCP exhibits a d -spacing 49.3%–53.7% shorter than the linear counterpart (*l*-BCP), in which the d -spacing reduction is considerably greater than experimental and theoretical results from the literature. Additionally, *tp-A*-BCP and *tp-B*-BCP exhibit 25.0%–32.5% shorter d -spacings than *l*-BCP. Overall, the cyclic and tadpole block copolymers form nanostructures with higher degrees of structural integrity and orientation than *l*-BCP. All the structural details are discussed in correlation with the molecular topology effects.

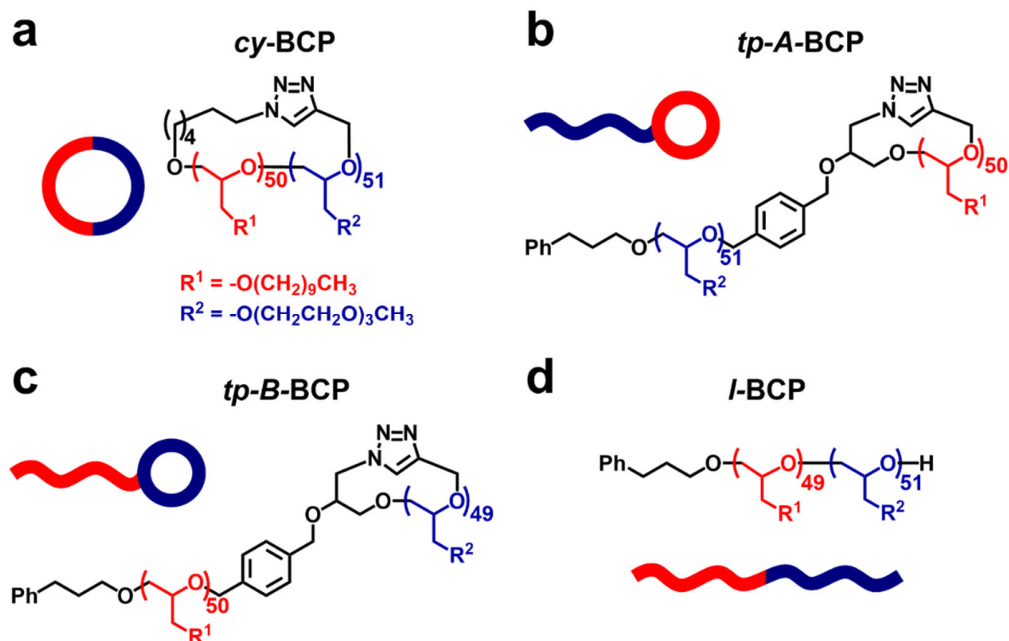


Figure 1. Chemical structures of cyclic and tadpole-shaped poly(*n*-decyl glycidyl ether-*block*-2-(2-(2-methoxyethoxy)ethoxy)ethyl glycidyl ether)s and their linear counterpart.

cy-BCP, *tp-A*-BCP, *tp-B*-BCP, and *l*-BCP were synthesized and characterized, as described in the literature.^{43,55} Their molecular characteristics are summarized in Table S1. All topological copolymers exhibit glass transitions below $-36.0\text{ }^\circ\text{C}$ and crystal melting points below $23.5\text{ }^\circ\text{C}$ (Figure S1 and Table S2). In this study, nanoscale films of each block copolymer were prepared through spin-coating onto silicon substrates with a 0.5 wt% polymer solution in tetrahydrofuran, which was filtered through a syringe equipped with a polytetrafluoroethylene filter membrane ($0.2\text{ }\mu\text{m}$ pores). The film thicknesses were found to be 100–120 nm after drying in vacuum at room temperature for 24 h. Individual films were stored in vacuum at room temperature prior to grazing-incidence small- and wide-angle X-ray scattering (GISAXS, GIWAXS) measurements, which were also conducted at room temperature. Because phase transitions occur below $23.5\text{ }^\circ\text{C}$, the prepared copolymer films were considered to be thermally annealed through the drying process and storage period.

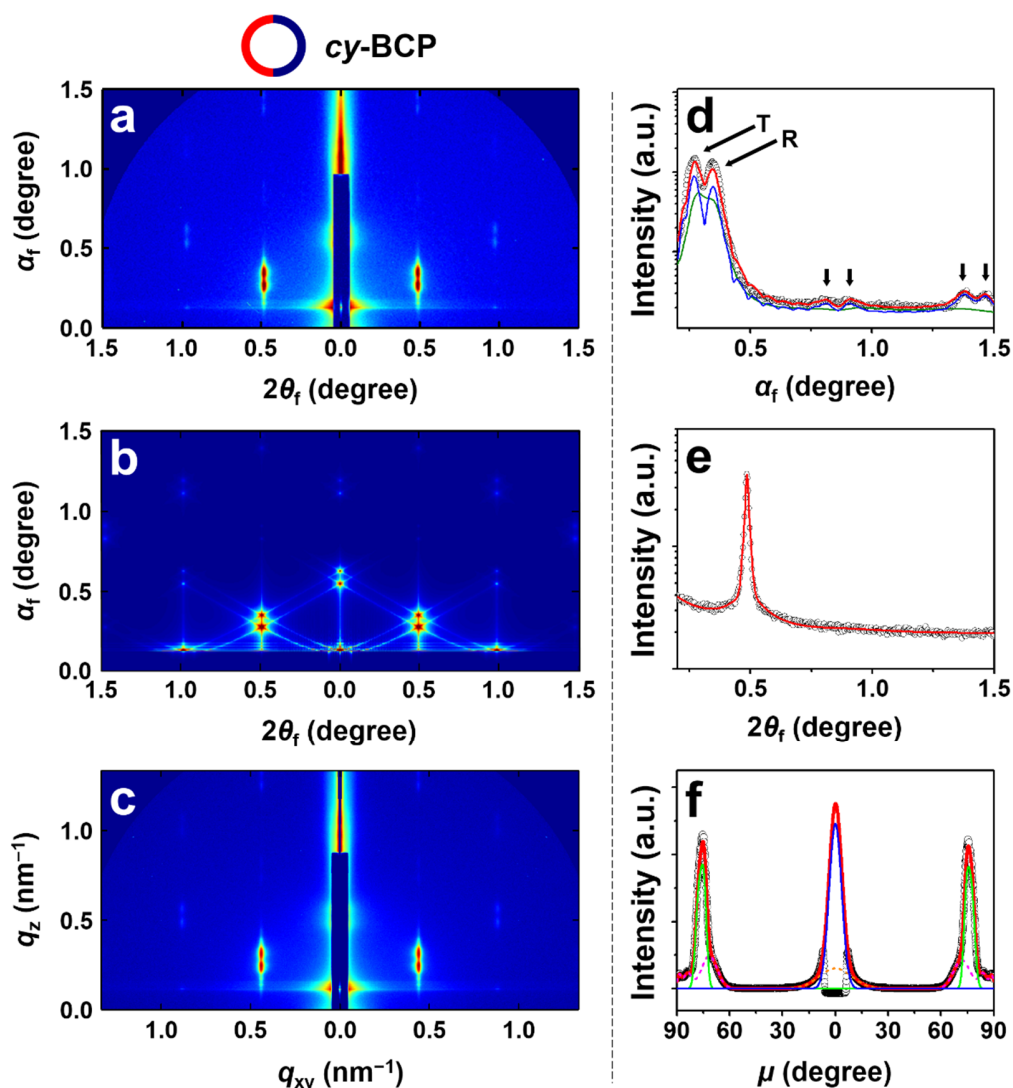


Figure 2. Representative GISAXS data of *cy*-BCP films (100–120 nm) measured at SDD = 2909.8 mm; $\alpha_i = 0.1276^\circ$ at room temperature using a synchrotron X-ray beam ($\lambda = 0.12095$ nm). (a) 2D scattering image in angle space. (b) Reconstructed 2D scattering image based on the structural parameters. (c) 2D scattering image in (a) reduced to scattering vector space. (d) 1D out-of-plane scattering profile along the meridian line at $2\theta_f = 0.485^\circ$ from (a), where the red line is the sum of calculated intensities of short-range ordered (green line) and long-range ordered (blue line) cylindrical domains (the scattering peaks generated by the reflected and transmitted X-ray beam are indicated as “R” and “T”, respectively). (e) 1D in-plane scattering profile along the equatorial line at $\alpha_f = 0.229^\circ$ from (a). In (d) and (e), open circles represent the measured scattering intensities and solid red lines are the calculated intensities based on the GIXS formula of hexagonal cylindrical structure model (see Supporting Information). (f) 1D azimuthal scattering profile from the azimuth at $q = 0.564 \text{ nm}^{-1}$ from (c) where the open circles are the measured data and the solid lines were obtained *via* data deconvolution: the blue and green solid lines are the scattering peaks of cylindrical domains in hexagonal packing order, the dashed magenta line corresponds to Yoneda peak, the dashed orange line is residual intensities from the reflected X-ray beam, and the red solid line is the total sum of all deconvoluted peaks.

A representative two-dimensional (2D) GIWAXS image of the *cy*-BCP nanoscale films (100–120 nm thick) is shown in Figures S2a and b. The GIWAXS data revealed two isotropic scattering peaks: one near 3.32° (2.09 nm *d*-spacing) and another at approximately 14.59° (0.476 nm *d*-spacing). The two peaks are commonly referred to as amorphous halos, which are also observed for *tp-A*-BCP, *tp-B*-BCP, and *l*-BCP (2D images not shown). The in-plane scattering profiles extracted from the measured data are compared in Figure S2c, in which the peak near 3° correlates to the mean interdistance between the polymer chains, and the peak near 15° corresponds to the mean intramolecular and intermolecular interdistances between *n*-decyl and 2-(2-(2-methoxyethoxy)ethoxy)ethyl bristles. Collectively, the GIWAXS measurements confirmed that the PDGE and PTEGGE blocks of all copolymers are amorphous in the nanoscale films at room temperature.

Figure 2a shows a representative GISAXS image of the *cy*-BCP films (100–120 nm) at room temperature; its *q*-space image is shown in Figure 2c. The image clearly reveals a hexagonal array of peaks, in which each peak appears as a pair split in the α_f axis direction. The peak splitting phenomenon occurs specifically for in-plane oriented (*i.e.* horizontal) nanostructures, and it implies that, based on GIXS optics, the above and below peaks are generated by the reflected and transmitted X-ray beams, respectively. In addition, from the specular reflection position, the relative scattering vector lengths of the peaks at $\alpha_f = 0.344^\circ$, 0.904° , and 1.460° occurring along the meridian line at $2\theta_f = 0.485^\circ$ are found to be 1, $\sqrt{3}$, and 2, respectively. These are typical scattering characteristics of horizontal hexagonally packed cylindrical structures. Considering this, we quantitatively analyzed the data in Figure 2a with the GIXS formula of the hexagonally packed cylinder model (details provided in Supporting Information and Figure S3), in which two-phase cylinders (core and shell) are surrounded by a matrix phase, derived for this study. The out-of-plane and the in-plane scattering profiles extracted along the median line at $2\theta_f = 0.485^\circ$ and equatorial line at $\alpha_f = 0.229^\circ$, respectively,

could be fitted reasonably well with the hexagonally packed cylinder model (Figures 2d and 2e). The analysis on the azimuthal scattering profile (Figure 2f) extracted at $q = 0.564 \text{ nm}^{-1}$ from the q -space image (Figure 2c) quantified the cylinder orientation with respect to the substrate. The structural parameters determined from the aforementioned analyses are summarized in Table 1. Based on the obtained structural parameters, a 2D GISAXS image was reconstructed through the GISAXS formula (Figure 2b), which agreed well with the measured data and confirmed successful data analysis.

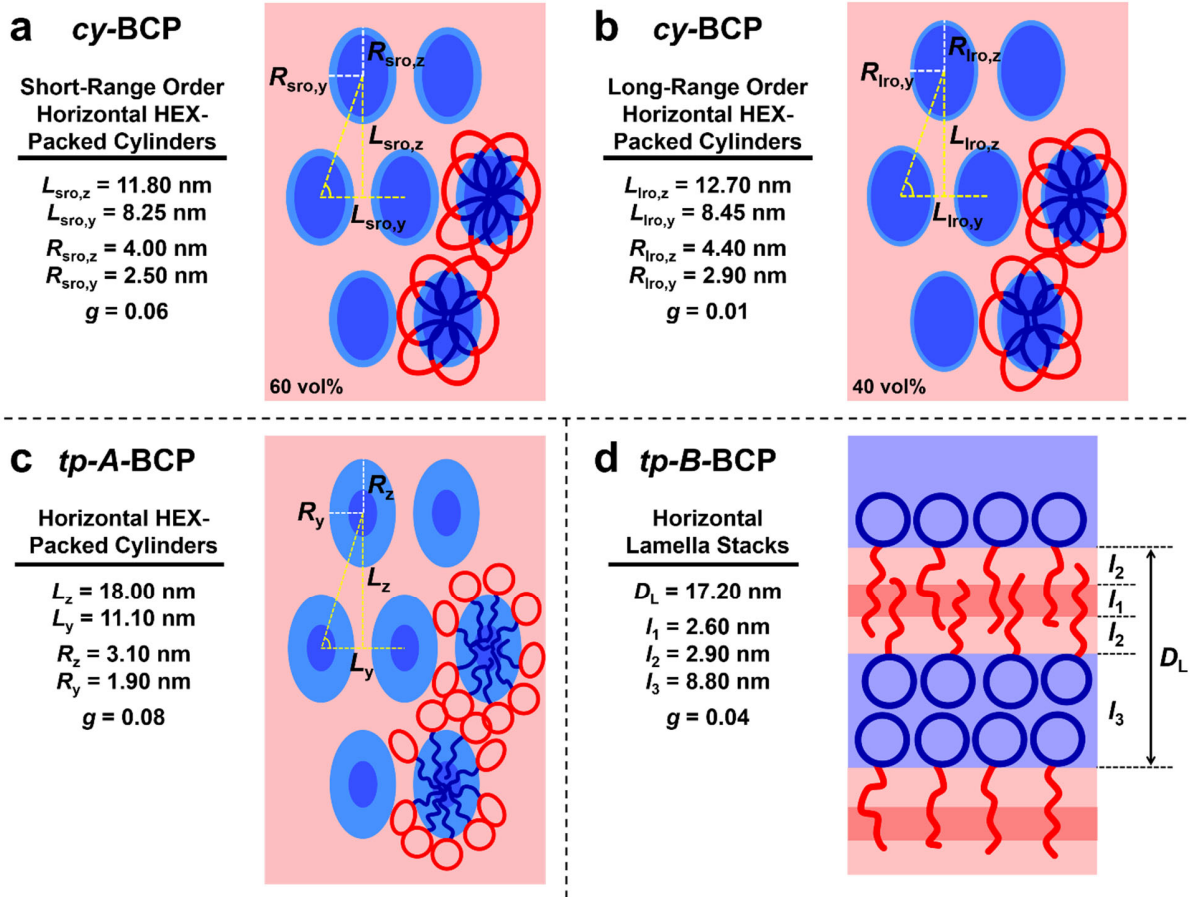






Figure 3. Schematic representations of nanostructures (cross-sectional view) inside topological block copolymer films. (a) Short-range order (60 vol%) and (b) long-range order (40 vol%) horizontal hexagonally-packed cylindrical structure inside *cy*-BCP film; for (a) and (b), the blue cylinder phase is assigned to PTEGGE block and the red matrix phase is assigned to PDGE block of *cy*-BCP. (c) Horizontal hexagonally-packed cylindrical structure inside *tp-A*-BCP film where the blue cylinder phase is assigned to linear PTEGGE block and the red matrix phase is assigned to cyclic PDGE block of *tp-A*-BCP. (d) Horizontal lamellar structure inside *tp-B*-BCP film where red sublayers l_1 and l_2 are formed by the linear PDGE block, and the blue sublayer l_3 is formed by the cyclic PTEGGE block of *tp-B*-BCP.

Table 1. Morphological parameters of nanoscale films (100–120 nm thick) of topological polymers

Nanoscale film morphology	Topological polymer			
	cy-BCP 	tp-A-BCP 	tp-B-BCP 	l-BCP 
<i>Hexagonal cylindrical structure</i>	horizontal	horizontal	horizontal	horizontal
	<i>short-range-order (sro)</i>	<i>long-range-order (lro)</i>		
L_z^a (nm)	11.80 (0.50) ^r	12.17 (0.50)	18.00 (1.22)	
L_y^b (nm)	8.25 (0.36)	8.45 (0.20)	11.10 (0.86)	
γ^c	1.43	1.50	1.62	
r_{cz}^d (nm)	4.00 (0.40)	4.40 (0.50)	3.10 (0.70)	
r_{cy}^e (nm)	2.50 (0.30)	2.90 (0.20)	1.90 (0.70)	
t_{sz}^f (nm)	0.70 (0.30)	0.50 (0.05)	4.10 (1.00)	
t_{sy}^g (nm)	0.80 (0.20)	0.40 (0.01)	2.50 (0.50)	
ε^h	1.42	1.49	1.64	
g^i	0.06	0.01	0.08	
ϕ^j (vol%)	60	40	100	
$\bar{\varphi}^k$ (deg.)	0		0	
σ_φ^l (deg.)	1.63		1.60	
O_s^m	0.994		0.994	
<i>Lamellar structure</i>			horizontal	horizontal vertical
D_L^n (nm)			17.20 (1.26)	24.00 (2.16) 25.50 (2.79)
l_1^o (nm)			2.60 (0.80)	9.40 (1.30) 9.00 (1.00)
l_2^p (nm)			2.90 (0.40)	2.50 (0.80) 3.60 (1.70)
l_3^q (nm)			8.80 (0.89)	9.60 (1.53) 9.30 (1.97)
g			0.04	0.33 0.35
$\bar{\varphi}$ (deg.)			0	0 90
σ_φ (deg.)			2.00	6.75 6.25
O_s			0.974	0.902 -0.210
ϕ (vol%)			100	50 50

^aMean interdistance between the arrays of the in-plane oriented cylindrical domains. ^bMean center-to-center distance of the cylindrical domains lain in the film plane. ^cRatio between L_z and L_y ($= L_z/L_y$). ^dCore radius of elliptical cylindrical domain along the z -axis which is parallel to the out-of-plane of the film. ^eCore radius of elliptical cylindrical domain along the y -axis which is parallel to the in-plane of the film. ^fShell thickness of elliptical cylindrical domain along the z -axis which is parallel to the out-of-plane of the film. ^gShell thickness of elliptical cylindrical domain along the y -axis which is parallel to the in-plane of the film. ^hElliptical axial ratio ($=$ polar radius/equatorial radius). ⁱParacrystal distortion factor of nanostructure (i.e., hexagonal cylinder structure or lamellar structure) along the z -axis which is parallel to the out-of-plane of the film. ^jVolume fraction in percent. ^kMean value of the polar angle φ (i.e., orientation angle) between the orientation vector \mathbf{n} set along a direction normal to the

{001} plane of horizontal hexagonal cylindrical structure or the in-plane of lamellar structure, and the out-of-plane direction of the film. ^lStandard deviation for the polar angle φ . ^mSecond-order orientation factor of nanostructure (i.e., hexagonal cylindrical structure or lamellar structure). ⁿLong period of lamellar structure. ^oThickness of the l_1 layer. ^pThickness of the l_2 layer. ^qThickness of the l_3 layer. ^rStandard deviation.

Interestingly, the quantitative analysis indicated two different levels of order existing within the *cy*-BCP film, the majority (60 vol%) of which exhibited a short-range order, and the rest (40 vol%) exhibited a long-range order (Figures 3a and b). The short-range order domain consisted of cylinders with elliptical cross-sections with a semi-major radius $R_{sro,z}$ of 4.70 nm [= 4.00 nm (core radius: r_{cz}) + 0.70 nm (shell thickness: t_{sz})] along the out-of-plane direction of the film (i.e. *z*-axis) and a semi-minor radius $R_{sro,y}$ of 3.30 nm [= 2.50 nm (r_{cy}) + 0.80 nm (t_{sy})] along the in-plane of the film (i.e. *y*-axis). Owing to the elliptical nature, the cylinders are positioned at non-conventional *d*-spacings, where L_z and L_y are 11.80 nm and 8.25 nm along the *z*- and *y*-axes, respectively. The lattice distortion factor *g* for the hexagonal arrangement of cylinders in the short-range order domain was 0.06. The long-range order domain consisted of elliptical cylinders with $R_{lro,z}$ of 4.90 nm and $R_{lro,y}$ of 3.30 nm. These elliptical cylinders were hexagonally packed with *d*-spacings of $L_z = 12.17$ nm and $L_y = 8.45$ nm, and the corresponding hexagonal lattice distortion factor *g* (*g*-factor) was 0.01. Such a low *g*-factor value indicates that the cylinders were exceptionally ordered in this domain. The sum of the short- and long-range order domains of the hexagonally packed cylinders was found to have a second-order orientation factor O_s of 0.994 and a mean polar angle $\bar{\varphi}$ of 0° (φ is the angle between the orientation vector ***n*** set normal to the {001} plane of the horizontal hexagonal cylinders as shown in Figure S4, and the out-of-plane direction of the film; $\sigma_\varphi = 1.63^\circ$, standard deviation for φ). Based on the structural parameters, the volume fraction of the cylinders was estimated to be 50.0% for the short-range order domain and 49.4% for the long-range order domains. Considering that the PDGE block in *cy*-BCP has a slightly higher volume fraction than that of the PTEGGE block, we could assign the cylinders and matrix comprising of the PTEGGE and PDGE blocks, respectively.

These are significant morphological features compared to *l*-BCP, which forms a mixture of horizontal and vertical lamellar structures (Figures S5, S6 and Table 1). The observed *d*-spacing reduction of *cy*-BCP was 49.3%–53.7% by comparing the L_z values of both the short- and long-range order domains against long periods (D_L) of *l*-BCP. This resulted in a greater reduction than the theoretical predictions⁴⁹⁻⁵¹ and experimental observations.^{46-48,53} In addition, *cy*-BCP cylindrical structure exhibits a considerably greater structural integrity and ordering, as indicated by the noticeable differences in the *g*-factor values ($g_{cy-BCP} = 0.01, 0.06$; $g_{l-BCP} = 0.33, 0.35$). The visual assessment (Figure 2a shows up to third-order peaks) and statistical evaluation ($g_{cy-BCP} = 0.01, 0.06$) of the cylindrical structure are noteworthy because it is uncommon to observe a well-defined polymer nanostructure to this degree inside nanoscale films. Furthermore, cylindrical structures formed by *cy*-BCP present a unidirectional orientation with O_s approaching unity, whereas *l*-BCP lamellae lack orientation control.

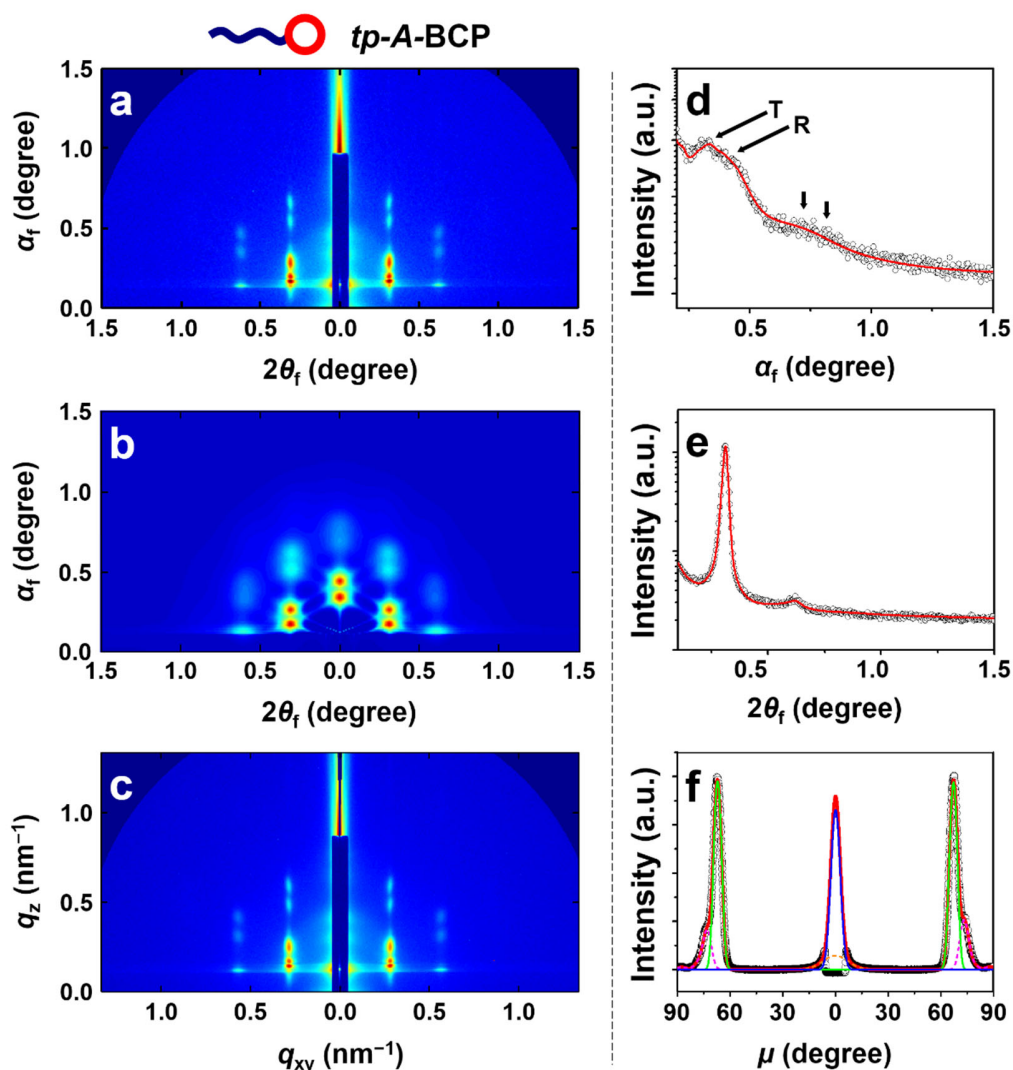


Figure 4. Representative GISAXS data of *tp-A-BCP* films (100–120 nm thick) measured at SDD = 2909.8 mm; $\alpha_i = 0.1361^\circ$ at room temperature using a synchrotron X-ray beam ($\lambda = 0.12095$ nm). (a) 2D scattering image in angle space. (b) Reconstructed 2D scattering image based on the structural parameters. (c) 2D scattering image in (a) reduced to scattering vector space. (d) 1D out-of-plane scattering profile along the meridian line at $2\theta_f = 0.101^\circ$ from (a), where the scattering peaks generated by the reflected and transmitted X-ray beam are indicated as “R” and “T”, respectively. (e) 1D in-plane scattering profile along the equatorial line at $\alpha_f = 0.192^\circ$ from the scattering image in (a). In (d) and (e), open circles represent the measured scattering intensities and solid red lines are the calculated intensities based on the GIXS formula of hexagonal cylindrical structure model (see Supporting Information). (f) 1D azimuthal scattering profile from the azimuth at $q = 0.417 \text{ nm}^{-1}$ from (c) where the open circles are the measured data and the solid lines were obtained *via* data deconvolution: the blue and green solid lines are the scattering peaks of cylindrical domains in hexagonal packing order, the dashed magenta line corresponds to Yoneda peak, the dashed orange line is residual intensities from the reflected X-ray beam, and the red solid line is the total sum of all deconvoluted peaks.

The GISAXS pattern of *tp-A*-BCP film in Figure 4a resembles that of *cy*-BCP with the hexagonal array of peaks and peak splitting. Using the hexagonally packed cylinder model, the out-of-plane and in-plane scattering profiles extracted along the median and equatorial lines at $2\theta_f = 0.101^\circ$ and $\alpha_f = 0.192^\circ$, respectively, could be fitted reasonably well (Figures 4d and e). The azimuthal scattering profile (Figure 4f) extracted at $q = 0.417 \text{ nm}^{-1}$ from Figure 4c was fitted to parameterize cylinder orientation. The structural parameters thus obtained are summarized in Table 1. The reconstructed 2D GISAXS image (Figure 4b) complied well with the measured data and confirmed successful data analysis. *tp-A*-BCP formed elliptical cylinders (Figure 3c) with the semi-major (R_z) and semi-minor (R_y) radii of 7.20 nm and 4.40 nm, respectively. The hexagonal arrangement of cylinders were defined by $L_z = 18.00 \text{ nm}$, $L_y = 11.00 \text{ nm}$, $g = 0.08$, and $O_s = 0.994$ ($\bar{\varphi} = 0^\circ$ and $\sigma_\varphi = 1.60^\circ$). Further, the cylinders revealed a volume fraction of 49.8%, implying that the linear PTEGGE block and the cyclic PDGE block formed the cylinders and the matrix, respectively.

The self-assembly of *tp-A*-BCP into a well-defined cylindrical structure with an excellent unidirectional orientation is a similar behavior exhibited by *cy*-BCP. However, the cylinders formed by *tp-A*-BCP are larger, positioned further apart, and relatively less ordered than those of *cy*-BCP ($g_{\text{cy-BCP}} = 0.01, 0.06$; $g_{\text{tp-A-BCP}} = 0.08$). Moreover, the 25.0%–29.4% *d*-spacing reduction compared to *l*-BCP corresponds with the theoretical predictions,⁴⁹⁻⁵¹ but this result is not directly applicable since the predictions are based on the cyclic topology.

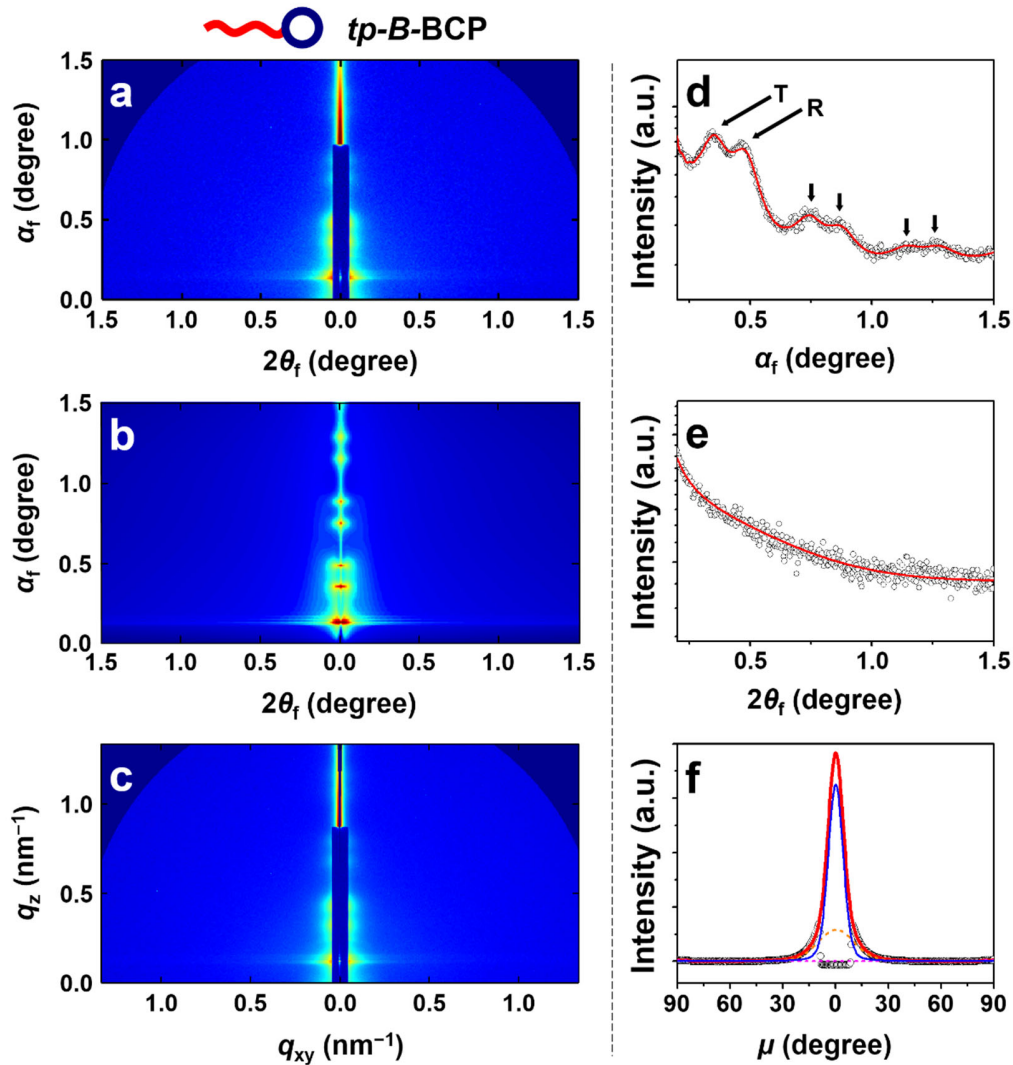


Figure 5. Representative GISAXS data of *tp-B-BCP* films (100–120 nm thick) measured at SDD = 2909.8 mm; $\alpha_i = 0.1353^\circ$ at room temperature using a synchrotron X-ray beam ($\lambda = 0.12095$ nm). (a) 2D scattering image in angle space. (b) Reconstructed 2D scattering image based on the structural parameters. (c) 2D scattering image in (a) reduced to scattering vector space. (d) 1D out-of-plane scattering profile along the meridian line at $2\theta_f = 0.117^\circ$ from (a), where the scattering peaks generated by the reflected and transmitted X-ray beam are indicated as “R” and “T”, respectively. (e) 1D in-plane scattering profile along the equatorial line at $\alpha_f = 0.202^\circ$ from (a). In (d) and (e), open circles represent the measured scattering intensities and solid red lines are the calculated intensities based on the GIXS formula of lamellar structure model (see Supporting Information). (f) 1D azimuthal scattering profile from the azimuth at $q = 0.430 \text{ nm}^{-1}$ from (c) where the open circles are the measured data and the solid lines were obtained *via* data deconvolution: the blue solid line is the first order scattering peak of lamellar structure, the dashed magenta line corresponds to Yoneda peak, the dashed orange line is residual intensities from the reflected X-ray beam, and the red solid line is the total sum of all deconvoluted peaks.

The *tp-B-BCP* film produced a 2D GISAXS pattern (Figure 5a) different from those of *tp-A-BCP* and *cy-BCP*, with three pairs of peaks appearing along the meridian line at $2\theta_f = 0^\circ$. Moreover,

relative scattering vector lengths of peaks at $\alpha_f = 0.460^\circ$, 0.868° , and 1.267° were 1, 2, and 3, respectively, from the specular reflection position. These are typical scattering characteristics of a horizontal lamellar structure. Moreover, the out-of-plane and in-plane scattering profiles extracted along the meridian and equatorial lines at $2\theta_f = 0.117^\circ$ and $\alpha_f = 0.202^\circ$, respectively, were satisfactorily fitted with the GIXS formula of the lamellar structure model prepared for this study (Figures 5d and e; see GIXS formula detail in Supporting Information and Figure S3). The lamellar orientation was evaluated from the azimuthal scattering profile (Figure 5f) extracted at $q = 0.430 \text{ nm}^{-1}$ from Figure 5c. The obtained structural parameters are summarized in Table 1, and they were utilized for the scattering image reconstruction (Figure 5b), which agrees well with the measured data. The horizontal lamellar structure (Figure 3d) has a long period D_L of 17.2 nm; sublayers l_1 , l_2 , and l_3 of 2.60 nm, 2.90 nm, and 8.80 nm, respectively; lamellar lattice g -factor of 0.04; and O_s of 0.974 ($\bar{\varphi} = 0^\circ$ and $\sigma_\varphi = 2.00^\circ$). For *tp-B-BCP*, the PTEGGE block had a slightly larger volume fraction than the PDGE block. Hence, the l_3 sublayer can be assigned by the cyclic PTEGGE block phase, whereas the sum of the l_1 and l_2 sublayers can be assigned to the linear PDGE block phase.

Interestingly, among all the topological copolymers used in this study, only *tp-B-BCP* exhibited a similar behavior to the aforementioned predictions⁴⁹⁻⁵¹ with additional features, despite possessing a tadpole topology. It achieved a 28.3%–32.5% d -spacing reduction compared to *l-BCP* in the same morphological type (lamellar), and showed a unidirectional horizontal orientation unlike the mixed orientation of *l-BCP* lamellae. Additionally, the lamellar ordering was significantly higher than *l-BCP*, as indicated by the statistical evaluation ($g_{tp-B-BCP} = 0.04$; $g_{l-BCP} = 0.33, 0.35$) and visual assessment (Figure 5a shows up to third-order peaks). The ordering of the *tp-B-BCP* lamellae was also higher than cylindrical structures of *tp-A-BCP* and *cy-BCP* (short-range order domain) but lower than that of the long-range order domain in the *cy-BCP* film.

Considering that the PDGE and PTEGGE blocks in all the copolymers possessed similar degrees of polymerization (~ 50) and volume fractions, the drastic differences in their morphological features among the linear, cyclic, and tadpole topologies were highly noteworthy. *tp-B*-BCP is the only copolymer to form the same nanostructure type (*i.e.* lamellar structure) as *l*-BCP. This suggests that in *tp-B*-BCP, which consists of linear PDGE block and cyclic PTEGGE block, the cyclized PTEGGE block does not significantly change its phase diagram when compared to *l*-BCP. In contrast, *cy*-BCP and *tp-A*-BCP form cylindrical structures, and both of their PDGE blocks are either fully cyclized or are a part of a macrocycle. Hence, the nonlinear topology of PDGE seemed to shift the phase diagram in comparison to *l*-BCP. The stark contrast in the sensitivity to the topological alteration between the PDGE and PTEGGE blocks may stem from their chemical structures. Although the polyether based backbone is shared by both blocks, PDGE and PTEGGE blocks differ in their side chain bristles. The *n*-decyl bristle in the PDGE blocks is a linear, saturated hydrocarbon with a sufficient length to exhibit a relatively greater stiffness (*i.e.* longer persistence length) than the flexible 2-(2-(2-methoxyethoxy)ethoxy)ethyl bristles of the PTEGGE blocks. Therefore, compared to the PTEGGE block, the PDGE block would experience a significant change in its chain conformation caused by the nonlinear topology, resulting in a significant shift in the phase diagram to yield cylindrical structures.

However, the cylindrical structures achieved by *cy*-BCP and *tp-A*-BCP are uniquely defined by their elliptical cylinders with elliptical axial ratios ε much greater than 1 ($\varepsilon_{cy\text{-BCP}} = 1.42, 1.49$; $\varepsilon_{tp\text{-A-BCP}} = 1.64$). In addition, their L_z/L_y ratios γ ($\gamma_{cy\text{-BCP}} = 1.43, 1.50$; $\gamma_{tp\text{-A-BCP}} = 1.62$) deviate significantly from $\sqrt{3}/2$, which is γ value for conventional cylindrical structures. These results indicate that both the shape and arrangement of the cylinders conform to non-conventional dimensions to retain the cylindrical structure with near-equivalent volume fractions between the cylinders and matrix. Overall,

the cyclic topology and related complex variations (*i.e.* tadpole and bicyclic), in conjunction to block configuration, critically influence the nanostructure type.

GISAXS characterization suggested that the cyclic and tadpole topologies increase the structural ordering as evidenced by significantly reduced g -factors for all topological copolymers compared to l -BCP. In cy -BCP, it can be theorized that the cyclic topology drastically improves structural ordering by the following rationale. Cyclic topology reduces the degree of freedom to the copolymer, yielding a more compact chain conformation. Consequently, both intra and intermolecular interactions among the same side chains for both blocks increase to generate a significant enthalpic gain, which promotes the formation of a highly ordered nanostructure. It appears that the enthalpic gain is sufficient to overcome the entropic loss of forming the long-range order domain with an exceptionally low g -factor of 0.01. For tp - A -BCP and tp - B -BCP, it is also speculated that the compact chain conformation of cyclized block extends its positive enthalpic influence to the linear block to establish the nanostructure ordering that corresponds with cy -BCP. These insights are, however, solely based on GISAXS characterization results, and further theoretical and experimental investigations are required to evaluate the extent of thermodynamic impact of a cyclic topology in detail.

In summary, the nanoscale film morphologies of cyclic and tadpole block copolymers, cy -BCP, tp - A -BCP, and tp - B -BCP, and their linear counterpart l -BCP, were investigated in detail for the first time using synchrotron GIXS analysis. The quantitative GIXS analysis provided structural details of the nanoscale film morphologies. Furthermore, the analysis provided critical correlations between the film morphology and molecular topology. All topological block copolymers revealed phase-separated nanostructures in which the nanostructure type was found to be highly dependent on the molecular topology, *i.e.* cy -BCP and tp - A -BCP form distorted hexagonally packed cylindrical structures, whereas tp - B -BCP and l -BCP form lamellar structures. Furthermore, the magnitude of nanostructure domain spacing was significantly dependent on the topology, *i.e.* cy -BCP < tp - B -BCP

$\approx tp-A$ -BCP $\ll l$ -BCP. Notably, cy -BCP achieved 49.3%–53.7% reduction in domain spacing than l -BCP. This reduction in domain spacing was greater than the theoretical predictions and previous experimental reports. $tp-A$ -BCP and $tp-B$ -BCP achieved domain spacing reductions of 25.0%–32.5% compared to l -BCP, which is comparable to both theoretical predictions and previous reports. Most importantly, cy -BCP, $tp-A$ -BCP, and $tp-B$ -BCP formed nanostructures with exceptionally high structural ordering and unidirectional horizontal orientation, unlike l -BCP, which exhibited poor ordering and low orientation control. Overall, this study demonstrated that both the cyclic and tadpole block copolymer approaches are powerful strategies for producing highly ordered, unidirectional, and miniaturized domain-based nanostructures.

Associated Content

Supporting Information

The Supporting Information is available free of charge at <https://pubs.acs.org/doi>

Sample preparation, synchrotron grazing-incidence X-ray scattering, grazing-incidence X-ray scattering data analysis, Table S1-S3, Figures S1-S5.

Author Information

Corresponding Author

Toshifumi Satoh – Faculty of Engineering, Hokkaido University, Sapporo 060-8628, Japan; Email: satoh@eng.hokudai.ac.jp

Authors

Brian J. Ree – Faculty of Engineering, Hokkaido University, Sapporo 060-8628, Japan;

Yusuke Satoh – Graduate School of Chemical Sciences and Engineering, Hokkaido University, Sapporo 060-8628, Japan;

Takuya Isono – Faculty of Engineering, Hokkaido University, Sapporo 060-8628, Japan;

Author Contributions

T.S. supervised the project. B.J.R., Y.S., and T.I. designed the experiments, solved the technical issues, and checked the experimental results. All authors contributed to developing the overall scope, interpreting the results and preparing the manuscript.

Notes

The authors declare no competing interests.

Acknowledgements

This study was supported by JSPS Grant-in-Aid for Scientific Research (A and B) (19H00905 and 19H02769 for T.S.), MEXT Grant-in-Aid for Scientific Research on Innovative Areas “Hybrid Catalysis” (20H04789 for T.S.), JSPS Grant-in-Aid for Challenging Exploratory Research (19K22209 for T.S.), JST CREST (JPMJCR19T4 for T.S.), the Photoexcitonix Project (Hokkaido University, T. S.), Creative Research Institute (CRIS, Hokkaido University, T. S.), and the Frontier Chemistry Center (Hokkaido University, T. S., T. I., and B. J. R.). B. J. R. was funded by the JSPS Fellowship for Young Scientists. The authors thank the Pohang Accelerator Laboratory for providing opportunities to conduct synchrotron X-ray scattering measurements.

REFERENCES

- (1) Patnode, W.; Wilcock, D. F. Methylpolysiloxanes. *J. Am. Chem. Soc.* **1946**, *68*, 358–363.
- (2) Hunter, M. J.; Hyde, J. F. Warrick, E. L.; Fletcher, H. J. Organo-Silicon Polymers. The Cyclic Dimethyl Siloxanes. *J. Am. Chem. Soc.* **1946**, *68*, 667–672.
- (3) Scott, D. W. Equilibria between Linear and Cyclic Polymers in Methylpolysiloxanes. *J. Am. Chem. Soc.* **1946**, *68*, 2294–2298.
- (4) Zimm, B. H.; Stockmayer, W. H. The Dimensions of Chain Molecules Containing Branches and Rings. *J. Chem. Phys.* **1949**, *17*, 1301–1314.
- (5) Fiers, W.; Sinsheimer, R. L. The Structure of the DNA of Bacteriophage ϕ X174: I. The Action of Exopolynucleotidases. *J. Mol. Biol.* **1962**, *5*, 408–419.
- (6) Fiers, W.; Sinsheimer, R. L. The Structure of the DNA of Bacteriophage ϕ X174: II. Thermal Inactivation. *J. Mol. Biol.* **1962**, *5*, 420–423.
- (7) Dulbecco, R.; Vogt, M. Evidence for A Ring Structure of Polyoma Virus DNA. *Proc. Natl. Acad. Sci. USA* **1963**, *50*, 236–243.

- (8) Weil, R.; Vinograd, J. The Cyclic Helix and Cyclic Coil Forms of Polyoma Viral DNA. *Proc. Natl. Acad. Sci. USA* **1963**, *50*, 730–738.
- (9) Witherup, K. M.; Bogusky, M. J.; Anderson, P. S.; Ramjit, H.; Ransom, R. W.; Wood, T.; Sardana, M. A Biologically Active, 31-Residue Cyclic Peptide Isolated from *Psychotria Longipes*. *J. Nat. Prod.* **1994**, *57*, 1619–1625.
- (10) Cascales, L.; Craik, D. J. Naturally Occurring Circular Proteins: Distribution, Biosynthesis and Evolution. *Org. Biomol. Chem.* **2010**, *8*, 5035–5047.
- (11) Dell, A.; Oates, J.; Lugowski, C.; Romanowska, E.; Kenne, L.; Lindberg, B. The Enterobacterial Common-Antigen, A Cyclic Polysaccharide. *Carbohydr. Res.* **1984**, *133*, 95–104.
- (12) Dodgson, K.; Semlyen, J. A. Studies of Cyclic and Linear Poly(dimethylsiloxanes): 1. Limiting Viscosity Number-Molecular Weight Relationships. *Polymer* **1977**, *18*, 1265–1268.
- (13) Hild, G.; Kohler, A.; Rempp, P. Synthesis of Ring-Shaped Macromolecules. *Eur. Polym. J.* **1980**, *16*, 525–527.
- (14) Roovers, J.; Toporowski, P. M. Synthesis of High Molecular Weight Ring Polystyrenes. *Macromolecules* **1983**, *16*, 843–849.
- (15) Kricheldorf, H. R.; Lee, S.-R.; Schittenhelm, N. Macrocycles, 1. Macrocyclic Polymerizations of (Thio)lactones—Stepwise Ring Expansion and Ring Contraction. *Macromol. Chem. Phys.* **1998**, *199*, 273–282.
- (16) Kricheldorf, H. R.; Eggerstedt, S. Macrocycles, 2. Living Macrocyclic Polymerization of ϵ -Caprolactone with 2,2-Dibutyl-2-stanna-1,3-dioxepane as Initiator. *Macromol. Chem. Phys.* **1998**, *199*, 283–290.
- (17) Hadjichristidis, N.; Pitsikalis, M.; Pispas, S.; Iatrou, H. Polymers with Complex Architecture by Living Anionic Polymerization. *Chem. Rev.* **2001**, *101*, 3747–3792.
- (18) Semlyen, J. A. *Cyclic Polymers*, 2nd ed. Kluwer Academic Publishers: Dordrecht, Netherlands, 2002.
- (19) Laurent B. A.; Grayson, S. M. Synthetic Approaches for the Preparation of Cyclic Polymers. *Chem. Soc. Rev.* **2009**, *38*, 2202–2213.
- (20) Kricheldorf, H. R. Cyclic Polymers: Synthetic Strategies and Physical Properties. *J. Polym. Sci. Part A: Polym. Chem.* **2010**, *48*, 251–284.
- (21) Jia, Z.; Monteiro, M. J. Cyclic Polymers: Methods and Strategies. *J. Polym. Sci. Part A: Polym. Chem.* **2012**, *50*, 2085–2097.

- (22) Xiang, L.; Ryu, W.; Kim, H.; Ree, M. Precise Synthesis, Properties, and Structures of Cyclic Poly(ϵ -caprolactone)s. *Polymers* **2018**, *10*, 577.
- (23) Liu, B.; Wang, H.; Zhang, L.; Yang, G.; Liu, X.; Kim, I. A Facile Approach for the Synthesis of Cyclic Poly(*N*-isopropylacrylamide) Based on An Anthracene–Thiol Click Reaction. *Polym. Chem.* **2013**, *4*, 2428–2431.
- (24) Ogawa, T.; Nakazono K.; Aoki D.; Uchida S.; Takata T. Effective Approaches to Cyclic Polymer from Linear Polymer: Synthesis and Transformation of Macromolecular [1]Rotaxane. *ACS Macro Lett.* **2015**, *4*, 343–347.
- (25) Wang, H.; Zhang, L.; Liu, B.; Han, B.; Duan, Z.; Qi, C.; Park, D.-W.; Kim, I. Synthesis of High Molecular Weight Cyclic Poly(ϵ -caprolactone)s of Variable Ring Size Based on A Light-Induced Ring-Closure Approach. *Macromol. Rapid Commun.* **2015**, *36*, 1646–1650.
- (26) Isono, T.; Sasamori, T.; Honda, K.; Mato, Y.; Yamamoto, T.; Tajima, K.; Satoh, T. Multicyclic Polymer Synthesis through Controlled/Living Cyclopolymerization of α,ω -Dinorbornenyl-Functionalized Macromonomers. *Macromolecules* **2018**, *51*, 3855–3864.
- (27) Mato, Y.; Honda, K.; Tajima, K.; Yamamoto, T.; Isono, T.; Satoh, T. A Versatile Synthetic Strategy for Macromolecular Cages: Intramolecular Consecutive Cyclization of Star-Shaped Polymers. *Chem. Sci.* **2019**, *10*, 440–446.
- (28) Yamamoto, T.; Hosokawa, M.; Nakamura, M.; Sato, S.-i.; Isono, T.; Tajima, K.; Satoh, T. Sato, M.; Tezuka, Y. Synthesis, Isolation, and Properties of All Head-to-Tail Cyclic Poly(3-hexylthiophene): Fully Delocalized Exciton over the Defect-Free Ring Polymer. *Macromolecules* **2018**, *51*, 9284–9293.
- (29) Durmaz, H.; Dag, A.; Hizal, G.; Tunca, U. Cyclic Homo and Block Copolymers Through Sequential Double Click Reactions. *J. Polym. Sci. Part A: Polym. Chem.* **2010**, *48*, 5083–5091.
- (30) Tezuka, Y. *Topological Polymer Chemistry: Progress of Cyclic Polymers in Syntheses, Properties and Functions*. World Scientific: Hackensack, NJ, USA, 2013.
- (31) Jacobson, H.; Stockmayer, W. H. Intramolecular Reaction in Polycondensations. II. Ring-Chain Equilibrium in Polydecamethylene Adipate. *J. Chem. Phys.* **1950**, *18*, 1607–1612.
- (32) Geiser, D.; Höcker, H. Synthesis and Investigation of Macrocyclic Polystyrene. *Macromolecules* **1980**, *13*, 653–656.
- (33) Prentis, J. J. Spatial Correlations in A Self-Repelling Ring Polymer. *J. Chem. Phys.* **1982**, *76*, 1574–1583.

- (34) Roovers, J. The Melt Properties of Ring Polystyrenes. *Macromolecules* **1985**, *18*, 1359–1361.
- (35) Lee, H. C.; Lee, H.; Lee, W.; Chang, T.; Roovers, J. Fractionation of Cyclic Polystyrene from Linear Precursor by HPLC at The Chromatographic Critical Condition. *Macromolecules* **2000**, *33*, 8119–8121.
- (36) Hur, K.; Winkler, R. G.; Yoon, D. Y. Comparison of Ring and Linear Polyethylene from Molecular Dynamics Simulations. *Macromolecules* **2006**, *39*, 3975–3977.
- (37) Hur, K.; Jeong, C.; Winkler, R. G.; Lacevic, N.; Gee, R. H.; Yoon, D. Y. Chain Dynamics of Ring and Linear Polyethylene Melts from Molecular Dynamics Simulations. *Macromolecules* **2011**, *44*, 2311–2315.
- (38) Qiu, X.-P.; Tanaka, F.; Winnik, F. M. Temperature-Induced Phase Transition of Well-Defined Cyclic Poly(*N*-isopropylacrylamide)s in Aqueous Solution. *Macromolecules* **2007**, *40*, 7069–7071.
- (39) Ren, J. M.; Satoh, K.; Goh, T. K.; Blencowe, A.; Nagai, K.; Ishitake, K.; Christofferson, A. J.; Yiapanis, G.; Yarovsky, I.; Kamigaito, M.; Qiao, G. G. Stereospecific Cyclic Poly(methyl methacrylate) and Its Topology-Guided Hierarchically Controlled Supramolecular Assemblies. *Angew. Chem. Int. Ed.* **2014**, *53*, 459–464.
- (40) Ishizu, K.; Ichimura, A. Synthesis of Cyclic Diblock Copolymers by Interfacial Condensation. *Polymer* **1998**, *39*, 6555–6558.
- (41) Schmidt, B. V. K. J.; Fechler, N.; Falkenhagen, J.; Lutz, J.-F. Controlled Folding of Synthetic Polymer Chains Through The Formation of Positionable Covalent Bridges. *Nat. Chem.* **2011**, *3*, 234–238.
- (42) Wan, X.; Liu, T.; Liu, S. Synthesis of Amphiphilic Tadpole-Shaped Linear-Cyclic Diblock Copolymers *via* Ring-Opening Polymerization Directly Initiating from Cyclic Precursors and Their Application as Drug Nanocarriers. *Biomacromolecules* **2011**, *12*, 1146–1154.
- (43) Isono, T.; Satoh, Y.; Miyachi, K.; Chen, Y.; Sato, S.-i.; Tajima, K.; Satoh, T.; Kakuchi, T. Synthesis of Linear, Cyclic, Figure-Eight-Shaped, and Tadpole Shaped Amphiphilic Block Copolyethers *via* *t*-Bu-P₄-Catalyzed Ring Opening Polymerization of Hydrophilic and Hydrophobic Glycidyl Ethers. *Macromolecules* **2014**, *47*, 2853–2863.
- (44) Satoh, Y.; Matsuno, H.; Yamamoto, T.; Tajima, K.; Isono, T.; Satoh, T. Synthesis of Well-Defined Three- and Four-Armed Cage-Shaped Polymers *via* “Topological Conversion” from Trefoil- and Quatrefoil- Shaped Polymers. *Macromolecules* **2017**, *50*, 97–106.

- (45) Shingu, T.; Yamamoto, T.; Tajima, K.; Isono, T.; Satoh, T. Synthesis of μ -ABC Tricyclic Mikroarm Star Polymer *via* Intramolecular Click Cyclization. *Polymers* **2018**, *10*, 877.
- (46) Zhu, Y. Q.; Gido, S. P.; Iatrou, H.; Hadjichristidis, N.; Mays, J. W. Microphase Separation of Cyclic Block Copolymers of Styrene and Butadiene and of Their Corresponding Linear Triblock Copolymers. *Macromolecules* **2003**, *36*, 148–152.
- (47) Takano, A.; Kadoi, O.; Hirahara, K.; Kawahara, S.; Isono, Y.; Suzuki, J.; Matsushita, Y. Preparation and Morphology of Ring-Shaped Polystyrene-block-polyisoprenes. *Macromolecules* **2003**, *36*, 3045–3050.
- (48) Lescanec, R. L.; Hajduk, D. A.; Kim, G. Y.; Ran, Y.; Yin, R.; Gruner, S. M.; Hoegen-Esch, T. E.; Thomas, E. L. Comparison of the Lamellar Morphology of Microphase-Separated Cyclic Block Copolymers and Their Linear Precursors. *Macromolecules* **1995**, *28*, 3485–3489.
- (49) Marko, J. F. Microphase Separation of Block Copolymer Rings. *Macromolecules* **1993**, *26*, 1442–1444.
- (50) Jo, W. H.; Jang, S. S. Monte Carlo Simulation of The Order–Disorder Transition of A Symmetric Cyclic Diblock Copolymer System. *J. Chem. Phys.* **1999**, *111*, 1712–1720.
- (51) Zhang, G.; Fan, Z.; Yang, Y.; Qiu, F. Phase Behaviors of Cyclic Diblock Copolymers. *J. Chem. Phys.* **2011**, *135*, 174902.
- (52) Lecommandoux, S.; Borsali, R.; Schappacher, M.; Deffieux, A.; Narayanan, T.; Rochas, C. Microphase Separation of Linear and Cyclic Block Copolymers Poly(styrene-*b*-isoprene): SAXS Experiments. *Macromolecules* **2004**, *37*, 1843–1848.
- (53) Poelma, J. E.; Ono, K.; Miyajima, D.; Aida, T.; Satoh, K.; Hawker, C. J. Cyclic Block Copolymers for Controlling Feature Sizes in Block Copolymer Lithography. *ACS Nano* **2012**, *6*, 10845–10854.
- (54) Ree, B. J.; Satoh, Y.; Isono, T.; Satoh, T. Bicyclic Topology Transforms Self-Assembled Nanostructures in Block Copolymer Thin Films. *Nano Lett.* **2020**, *20*, 6520–6525.
- (55) Ree, B. J.; Satoh, Y.; Jin, K. S.; Isono, T.; Kim, W. J.; Kakuchi, T.; Satoh, T.; Ree, M. Well-Defined Stable Nanomicelles Self-Assembled by Brush Cyclic and Tadpole Copolymer Amphiphiles: A Versatile Smart Carrier Platform. *NPG Asia Mater.* **2017**, *9*, e453.

Table of Contents graphic

Highly Ordered Nanoscale Film Morphologies of Block Copolymers Governed by Nonlinear Topologies

*Brian J. Ree, Yusuke Satoh, Takuya Isono, and Toshifumi Satoh**

